ACS NANO

www.acsnano.org

M_5X_4: A Family of MXenes

Marley Downes, Christopher E. Shuck, Robert W. Lord, Mark Anayee, Mikhail Shekhirev, Ruocun John Wang, Tetiana Hryhorchuk, Martin Dahlqvist, Johanna Rosen, and Yury Gogotsi*

Cite This: *ACS Nano* 2023, 17, 17158−17168

Read Online

ACCESS | Metrics & More | Article Recommendations | Supporting Information

ABSTRACT: MXenes are two-dimensional (2D) transition metal carbides, nitrides, and carbonitrides typically synthesized from layered MAX-phase precursors. With over 50 experimentally reported MXenes and a near-infinite number of possible chemistries, MXenes make up the fastest-growing family of 2D materials. They offer a wide range of properties, which can be altered by their chemistry (M, X) and the number of metal layers in the structure, ranging from two in M_2XT_x to five in $M_5X_4T_x$. Only one M_5X_4 MXene, Mo_4VC_4, has been reported. Herein, we report the synthesis and characterization of two M_5AX_4 mixed transition metal MAX phases, $Ti_{2.5}Ta_{2.5}AlC_4$ and $Ti_{2.675}Nb_{2.325}AlC_4$, and their successful topochemical transformation into $Ti_{2.5}Ta_{2.5}C_4T_x$ and $Ti_{2.675}Nb_{2.325}C_4T_x$ MXenes. The resulting MXenes were delaminated into single-layer flakes, analyzed structurally, and characterized for their thermal and optical properties. This establishes a family of M_5AX_4 MAX phases and their corresponding MXenes. These materials were experimentally produced based on guidance from theoretical predictions, leading to more exciting applications for MXenes.

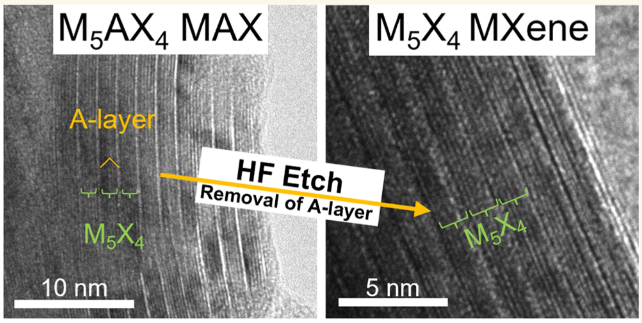

KEYWORDS: *MXene, two-dimensional, MAX phase, synthesis, structure, properties*

INTRODUCTION

MXenes are a large family of 2D materials, with more than 50 stoichiometric MXenes experimentally synthesized, hundreds of computationally predicted compositions, and an infinite number of solid-solution MXenes (Figure 1).[1,2] The general formula of MXenes can be expressed as $M_{n+1}X_nT_x$ where M is an early transition metal (Ti, Nb, Ta, Mo, V, etc.), X is carbon and/or nitrogen, and n is an integer 1−4. T_x represents the surface termination groups (typically −OH, =O, and −F)[3] and will not be continually expressed for clarity. MXenes have attracted significant attention due to their coupled high volumetric capacitance[4] and high electronic conductivity,[5] biocompatibility,[6] electrochromic behavior,[7] and optical absorption peaks in the UV−NIR range;[8] this has led to their use in applications including electrochemical energy storage,[9] biomedicine,[10] optoelectronics,[11] and many others.[12,13]

MXenes are commonly synthesized through selective chemical etching from precursor MAX phases, which have the general formula $M_{n+1}AX_n$, where the A layer is composed of group 13/14 elements (typically, Al for MXene synthesis). The monatomic A layer is removed during the chemical etching process, leaving behind multilayer (ML) MXene flakes.[14] Delamination with organic or inorganic ions can separate the multilayer MXene particles, yielding single flakes dispersed in water, which are easily processed into films through vacuum filtration, spray-coating, spin-coating, or other methods.[15,16]

While MXenes have the general formula $M_{n+1}X_nT_x$, the metallic component (M) can include two or more metals. Generally, these MXenes can be divided into ordered MXenes or solid-solution MXenes.[2] The ordered MXenes exhibit ordering in one of two ways: in-plane (*i*-MXene) or out-of-plane ordering (*o*-MXene). In-plane ordering is only found in $(M'_{4/3}M''_{2/3})CT_x$ structures (M' = Mo, W, V, Cr; M'' = Sc, Zr, Y, or some lanthanides)[39] and has alternating rows of the M-metals within the planes. Out-of-plane ordering is found in the $M'_2M''C_2T_x$ and $M'_2M''_2C_3T_x$ structures with M' in the outer layer and M'' in the inner layer(s), such as $Mo_2Ti_2C_3T_x$, $Mo_2TiC_2T_x$, $Mo_2ScC_2T_x$, or $Cr_2TiC_2T_x$.[40] Solid-solution MXenes, on the other hand, have random ordering of either the X-site or the M-site. Solid solution on the X site includes MXenes such as Ti_3CN, where the carbon and nitrogen randomly occupy the octahedral sites typically only occupied by carbon.[41] Solid solution on the M-site contains MXenes

Received: June 2, 2023
Accepted: August 25, 2023
Published: August 31, 2023

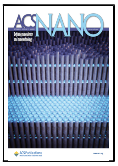

ACS Publications

https://doi.org/10.1021/acsnano.3c04967

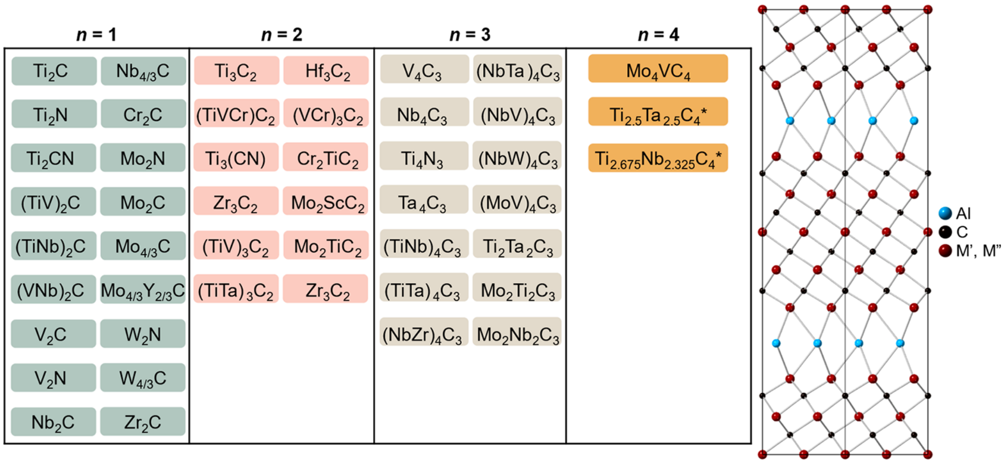

$n = 1$		$n = 2$		$n = 3$		$n = 4$
Ti_2C	$Nb_{4/3}C$	Ti_3C_2	Hf_3C_2	V_4C_3	$(NbTa)_4C_3$	Mo_4VC_4
Ti_2N	Cr_2C	$(TiVCr)C_2$	$(VCr)_3C_2$	Nb_4C_3	$(NbV)_4C_3$	$Ti_{2.5}Ta_{2.5}C_4$*
Ti_2CN	Mo_2N	$Ti_3(CN)$	Cr_2TiC_2	Ti_4N_3	$(NbW)_4C_3$	$Ti_{2.675}Nb_{2.325}C_4$*
$(TiV)_2C$	Mo_2C	Zr_3C_2	Mo_2ScC_2	Ta_4C_3	$(MoV)_4C_3$	
$(TiNb)_2C$	$Mo_{4/3}C$	$(TiV)_3C_2$	Mo_2TiC_2	$(TiNb)_4C_3$	$Ti_2Ta_2C_3$	
$(VNb)_2C$	$Mo_{4/3}Y_{2/3}C$	$(TiTa)_3C_2$	Zr_3C_2	$(TiTa)_4C_3$	$Mo_2Ti_2C_3$	
V_2C	W_2N			$(NbZr)_4C_3$	$Mo_2Nb_2C_3$	
V_2N	$W_{4/3}C$					
Nb_2C	Zr_2C					

Figure 1. Synthesized MXenes reported to date, including 18 M_2X,[5,17−26] 12 M_3X_2,[1,26−31] 14 M_4X_3,[26,27,30,32−35] and three M_5X_4.[36] Beyond these listed MXenes are in-plane ordered, various solid-solution compositions, high-entropy, and other related materials.[30,37,38] Two MXenes with $n = 4$ are reported here and are marked with stars. Additional MAX phases discovered in this study but not exfoliated into MXenes are shown in the Supporting Information. The crystal structure of the M_5AX_4 lattice with space group $P6_3/mmc$ is shown along the [110] plane.

that have a random occupation of the M-sites. M-site solid solution is the largest predicted family, as there are a near-infinite number of combinations across the periodic table to create MXenes. A large variety of solid-solution MXenes have been reported, including $Ti_{2-y}Nb_yCT_x$, $Ti_{2-y}V_yCT_x$,[5] and $Mo_{4-y}V_yC_3T_x$,[42] among many others. To date, $M_5X_4T_x$ MXene has only an M-site solid-solution structure.

MXenes are further divided into families based on the number of atomic layers: M_2X, M_3X_2, M_4X_3, and, most recently, M_5X_4. The first phase-pure higher-ordered MAX phase ($n > 3$) was reported in 2019 to be Mo_4VAlC_4 with accompanying MXene Mo_4VC_4, establishing that phase-pure higher-ordered MAX phases and MXenes could be successfully synthesized.[36] This family of MXenes is important because M_5X_4 ($n = 4$) demonstrates properties that are not found in other MXenes ($n = 1−3$). It was shown that they have the highest thermal stability of any MXene to date (~1000 vs <800 °C for other MXenes).[43,44] They do not have a plasmon resonance in the visible region, as compared to other MXenes, which have characteristic plasmon resonances from the near-UV to mid-IR.[8] Their conductivity is not significantly affected by intercalants, unlike all other MXenes.[45] Moreover, due to their atomically thicker nature, it is expected that their bending rigidity will allow them to keep a planar shape in suspended membranes, cantilevers, or polymer−matrix composites, exceeding all other 2D materials.[46,47] Mo_4VC_4 has recently found its first application as a nanotherapeutic agent against MRSA infection.[48] Following the synthesis of $(Ti_{0.5}Nb_{0.5})_5AlC_4$, Mo_4VAlC_4, and Mo_4VC_4, it was demonstrated that $n = 4$ was possible; however, it was unknown whether more MAX phases (and subsequent MXenes) could be synthesized.[36,49]

The theoretical design of MAX phases (and subsequent MXenes) is possible through density functional theory (DFT) calculations. Stable MAX phases can be predicted by modeling their enthalpies of formation and comparing those against competing MAX phases. For instance, the experimental synthesis of Mo_2ScAlC_2 was achieved by theoretically modeling the successful phase, despite its single-M derivatives being unstable (Mo_3AlC_2 and Sc_3AlC_2).[31] The first *i*-MAX-phase, $(Mo_{2/3}Sc_{1/3})_2AlC$, was used as a basis for the theoretical modeling and experimental verification of several *i*-MAX phases including $(V_{2/3}Zr_{1/3})_2AlC$ and $(Mo_{2/3}Y_{1/3})_2AlC$.[50] Theoretical models such as this allow for the accurate prediction of previously unattainable MAX-phase families and hundreds of theoretically possible MXenes.

Herein, we report two M_5AX_4 MAX phases: $Ti_{2.5}Ta_{2.5}AlC_4$ and $Ti_{2.675}Nb_{2.325}AlC_4$. The structural analysis found that $Ti_{2.5}Ta_{2.5}C_4$ shares the same herringbone-type structure as Mo_4VC_4, indicating that this structure may be characteristic of the M_5X_4 family. Optical and thermal analyses show promising properties not found in other MXenes, and the use of DFT to successfully predict stable MAX phases shows promise for expanding the M_5X_4 family.

RESULTS AND DISCUSSION

Synthesis and Structural Characterization. To find M_5AX_4 MAX phases, metal powder precursors were mixed in $M'_x{:}M''_{5-x}$ ratios where $x = 1$, 2, 2.5, 3, or 4. Each chemistry was tested with 5 at. % of one of the corresponding metallic oxides (see Supporting Information for a complete list of tested chemistries). Following ball-milling with zirconia balls, the powders were sintered at 1650 °C for 24 h under Ar. The products were characterized via powder X-ray diffraction (XRD). It was determined that of the chemistries tested the following yielded M_5AX_4 MAX phases: $Ti_{2.5}Ta_{2.5}AlC_4$ (using TiO_2) and $Ti_{2.675}Nb_{2.325}AlC_4$ (using Nb_2O_5). It may be the case that the use of oxides in synthesis results in oxygen dissolution in the carbon sublattice, forming oxycarbides[51] and stabilizing the structure; however, this will not be investigated in depth in this article. After the discovery of $Ti_{2.5}Ta_{2.5}AlC_4$ and $Ti_{2.675}Nb_{2.325}AlC_4$, DFT calculations were employed to confirm the stability of $Ti_{2.5}Ta_{2.5}AlC_4$ and $Ti_{2.675}Nb_{2.325}AlC_4$ as well as to predict the stability of other M_5AX_4 MAX phases. Details of DFT calculations are discussed later in this article. We experimentally tested the compositions that were predicted to be stable using the same metal−oxide ratios, which did not yield another M_5AX_4 MAX phase. However, we discovered a series of solid-solution compositions, such as $(TiTa)_2AlC$ and $(TaV)_2AlC$,[52] and alternate synthesis methods for preexisting MAX phases such as $(TiNb)_4AlC_3$, $(VNb)_4AlC_3$, and $(TiV)_2AlC$ (Table S1). These MAX phases were not used

https://doi.org/10.1021/acsnano.3c04967
ACS Nano 2023, 17, 17158−17168

for MXene synthesis in this work but represent a broad selection of solid-solution MAX phases and consequent MXenes for future study.

To synthesize multilayer MXene, HCl-washed MAX powders were etched with hydrofluoric acid (HF) to selectively etch the A layer. The process of optimizing the synthesis can be found in Figure S18. It was found that the optimal etching time was 9 days for $Ti_{2.5}Ta_{2.5}AlC_4$ and 7 days for $Ti_{2.675}Nb_{2.325}AlC_4$; these gave the highest yield without overetching. For analysis, the multilayer sediment was collected via vacuum-assisted filtration and dried at 25 °C.

Figure 2 shows an XRD analysis of the parent MAX phase as well as the derived MXenes. For $Ti_{2.5}Ta_{2.5}AlC_4$, the (002) peak occurs at 6.10°, corresponding to a *c*-lattice parameter of 28.85 Å; for $Ti_{2.675}Nb_{2.325}AlC_4$, the (002) peak occurs at 5.98° (*c*-lattice parameter of 28.88 Å), which is the largest *c*-lattice parameter of any known MAX phase.[36] Both are larger than the previously reported Mo_4VAlC_4 (28.22 Å) due to the larger ion sizes of both Ta and Nb in $Ti_{2.5}Ta_{2.5}AlC_4$ and $Ti_{2.675}Nb_{2.325}AlC_4$. The use of HF to selectively etch the A-layer resulted in the (002) peak shifting to lower 2*θ* for both, indicating the expansion along the *c*-lattice as a result of the A-layer removal.[44] Delamination of the multilayer MXenes was done by intercalating tetramethylammonium hydroxide (TMAOH) between the MXene sheets.[14] This was performed at both 25 and 35 °C; delaminated MXene from the 35 °C delamination was used for further analysis. For both MXenes, delamination only occurred when the dried multilayer powders were redispersed in the aqueous solution; delamination directly after etching and washing did not yield MXene but rather a light brown solution. For $Ti_{2.5}Ta_{2.5}C_4$, delamination occurred at both temperatures, with the average flake size increasing at higher temperatures (Figure S21); however, $Ti_{2.675}Nb_{2.325}C_4$ did not yield MXene at room temperature, suggesting stronger interactions between the MXene sheets. The longer etching time of $Ti_{2.5}Ta_{2.5}C_4$ contributed to minor defects in the MXene sheets, likely resulting in weaker interactions between the flakes, which allowed for delamination at a lower temperature (Figure S23). As seen in Figure 2, the delamination of multilayer powder resulted in another shift of the (002) peaks toward lower 2*θ* values and a broadening of the peaks, resulting from the semirandom flake alignment in the films.

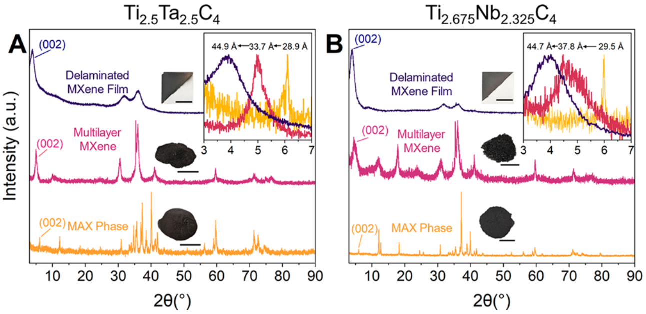

Figure 2. X-ray diffraction (XRD) patterns of (A) $Ti_{2.5}Ta_{2.5}C_4$ and (B) $Ti_{2.675}Nb_{2.325}C_4$ MAX, multilayer MXene, and delaminated MXene films with labeled (002) peaks. Insets show optical pictures of corresponding powders/spray-coated films. The scale bars on each image are 1 cm. Inset graphs show the (002) peak shift and the corresponding change in the *c*-lattice parameter.

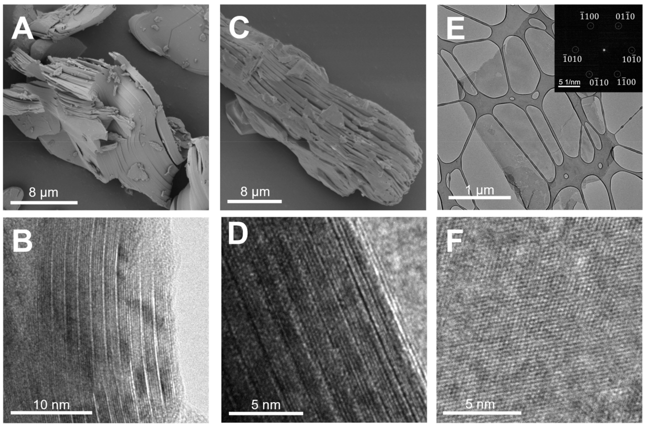

Figure 3. Microscopic analysis of $Ti_{2.675}Nb_{2.325}AlC_4$ and $Ti_{2.675}Nb_{2.325}C_4$. (A) Scanning electron microscopy (SEM) micrograph of $Ti_{2.675}Nb_{2.325}AlC_4$ MAX-phase particles. (B) Cross-sectional transmission electron microscopy (TEM) image showing the five-layered structure of $Ti_{2.675}Nb_{2.325}AlC_4$. The bright gray lines are the aluminum layers separating the five gray mixed-metal layers. (C) SEM micrograph of multilayer $Ti_{2.675}Nb_{2.325}C_4$ MXene showing increased gaps between layers indicating the selective etching and removal of the Al layer. (D) Cross-sectional TEM image showing a five-layered repeating structure of multilayer $Ti_{2.675}Nb_{2.325}C_4$ MXene. (E) In-plane TEM image of a large delaminated $Ti_{2.675}Nb_{2.325}C_4$ MXene flake folded in half on top of a lacey carbon grid with the hexagonal selected area electron diffraction (SAED) pattern of the [0001] zone axis in the inset. (F) HR-TEM image of the hexagonal atom arrangement in the basal plane of $Ti_{2.675}Nb_{2.325}C_4$ MXene.

Figure 3 shows the microscopic characterization of $Ti_{2.675}Nb_{2.325}AlC_4$ and $Ti_{2.675}Nb_{2.325}C_4$, where a visual indication of etching can be observed (Figure S23 for corresponding $Ti_{2.5}Ta_{2.5}C_4$ data). The expansion of the layers between the SEM micrographs in Figure 3A and C is indicative of Al removal from the MAX. This can be seen on the atomic level in the HR-TEM images (Figure 3B and D), where the brighter lines represent the Al layers. Their absence in the postetching image is visual proof of the selective removal of the A-layer, while the five-layered repeating MXene structure remains. The herringbone-type structure seen in Mo_4VAlC_4 was also observed in $Ti_{2.5}Ta_{2.5}AlC_4$ (Figure S23),[36] but Rietveld refinement of the XRD patterns reveals that both $Ti_{2.5}Ta_{2.5}AlC_4$ and $Ti_{2.675}Nb_{2.325}AlC_4$ fit the $P6_3/mmc$ structure better than the herringbone-type $P\bar{6}c2$ and $P\bar{6}m2$ structures (Figures S29, S30).[53] Further analysis is required to fully resolve the structure of these M_5AX_4 MAX phases. As the second example of this structure, the atomic arrangement may be characteristic of the M_5X_4 family as a more stable configuration. The $Ti_{2.675}Nb_{2.325}C_4$ MXene flake seen in Figure 3E is large enough to fold over itself, where the seam can be seen on the right side of the flake and non-overlapping sections can be seen on the left.

Unfolded, the flake in Figure 3E would be approximately 4.5 *μ*m wide and 2 *μ*m tall. This is larger than the average ~500 nm flake size recorded by dynamic light scattering (DLS) (Figure S21), showing that larger flake sizes are possible for $Ti_{2.675}Nb_{2.325}C_4$, indicating that increased stiffness relative to atomically thinner MXenes may lead to larger possible flake sizes.[54] On the other hand, $Ti_{2.5}Ta_{2.5}C_4$ showed flake sizes corresponding to the DLS flake measurements of ~300 nm (Figure S23). The SAED in Figure 3E corresponds to the hexagonal crystal structure, as viewed from the [0001] zone axis, confirming that the carbide crystal structure was

https://doi.org/10.1021/acsnano.3c04967
ACS Nano 2023, 17, 17158−17168

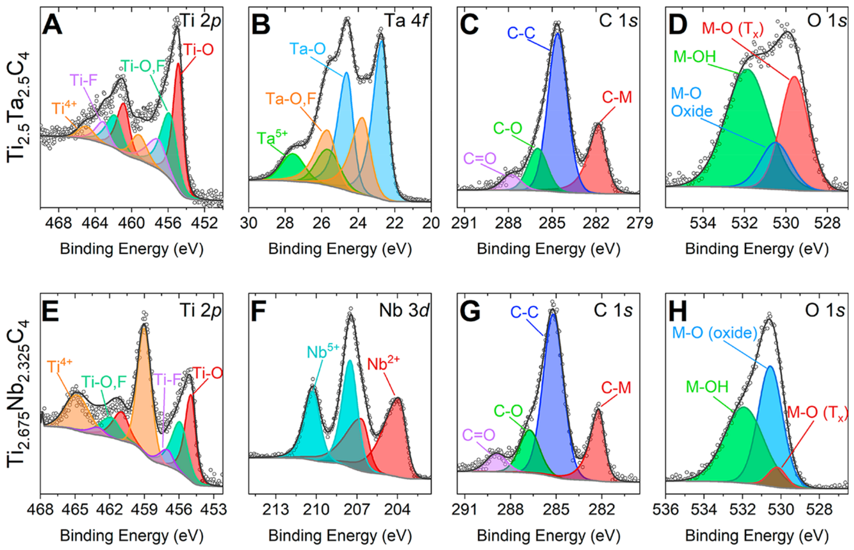

Figure 4. High-resolution X-ray photoelectron spectroscopy (XPS) spectra of (top) $Ti_{2.5}Ta_{2.5}C_4$ and (bottom) $Ti_{2.675}Nb_{2.325}C_4$ free-standing films, showing (A, E) Ti 2p, (C, G) C 1s, (D, H) O 1s, (B) Ta 4f, and (F) Nb 3d core-level spectra.

maintained during MXene synthesis. Atomic force microscopy (AFM) (Figure S22) demonstrates an average flake thickness of 3.4 nm for $Ti_{2.675}Nb_{2.325}C_4$, apparently overestimating the thickness due to entrapped solvent molecules.[44]

Compositional Characterization. Compositional characterization was carried out with both XPS for the delaminated MXene film (Figure 4), and EDS was conducted for MAX-phase, multilayer, and single-flake MXene (Table S5). XPS indicated a slight titanium deficiency in both MXenes; however, EDS indicated that the ratio was approximately equivalent to the initial stoichiometry amounts across all MAX and MXene stages. This may indicate a slight preferential ordering of titanium in the inner layers of the M_5X_4 unit cell, resulting in some of the titanium signal being blocked by the heavier metal in the outer layers. In $Ti_{2.5}Ta_{2.5}C_4$ this claim is further supported by the increased presence of oxygen over fluorine terminations, as tantalum preferentially bonds to oxygen. The lack of continual lattice fringes in the TEM images (Figures 3, S23) could indicate that both $Ti_{2.5}Ta_{2.5}C_4$ and $Ti_{2.675}Nb_{2.325}C_4$ do not have long-range order in both MAX phase and MXene. XPS also shows the metal−carbon bonds for both $Ti_{2.5}Ta_{2.5}C_4$ and $Ti_{2.675}Nb_{2.325}C_4$, confirming the MXene structure after synthesis. The presence of the M−O peaks can indicate either sample oxidation or the presence of an oxycarbide. While unconfirmed, the requirement of oxide for the successful M_5AX_4 MAX-phase synthesis may indicate that a small percentage of oxygen is needed to stabilize the lattice.

The Raman spectra of $Ti_{2.5}Ta_{2.5}AlC_4$ and $Ti_{2.675}Nb_{2.325}AlC_4$ MAX and $Ti_{2.5}Ta_{2.5}C_4$ and $Ti_{2.675}Nb_{2.325}C_4$ MXene in Figure 5 showed broad peaks below 1000 cm^{-1}, similar to the previously reported M_5X_4 MAX and MXene.[36] In the MAX spectra, the lack of signatures from Nb_2O_5 and TiO_2 precursors indicates complete reactions during the solid-state synthesis.[55,56] In both cases of the $Ti_{2.5}Ta_{2.5}C_4$ and $Ti_{2.675}Nb_{2.325}C_4$ systems, the MAX and MXene have similar Raman spectra. The Raman peaks are broad compared to the single-transition-metal MAX phases and ordered MXenes, which are indicative of disorder due to the solid solution of transition metals.[57,58] Moreover, $Ti_{2.5}Ta_{2.5}C_4$ showed more broadening than $Ti_{2.675}Nb_{2.325}C_4$ due to the greater difference

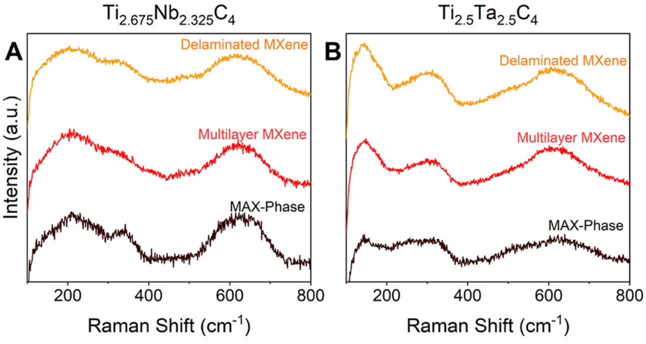

Figure 5. Raman spectra during each major synthesis step. (A) $Ti_{2.5}Ta_{2.5}C_4$ MAX and MXene spectra. (B) $Ti_{2.675}Nb_{2.325}C_4$ MAX and MXene spectra.

in atomic masses of the interchangeable elements. The peak between 100 and 400 cm^{-1} contains the vibrations of the transition metals and carbon. Compared to the MAX phases, the changes between 200 and 400 cm^{-1} in MXenes are attributed to the surface group vibrations, corresponding to ═O, −OH, and −F values shown by X-ray photoelectron spectroscopy (XPS) in Figure 4. The peak in $Ti_{2.5}Ta_{2.5}C_4$ showed a lower wavenumber than $Ti_{2.675}Nb_{2.325}C_4$, due to the heavier atoms. The final peak is located in the 600−700 cm^{-1} region where both in- and out-of-plane carbon vibrations are present. These peaks confirm the MXene structure and the absence of oxidation, as no signature of the relevant oxides was found in the same region. The full spectrum (Figure S26) showed a broad peak between 1000 and 1500 cm^{-1}. Since MXenes do not possess a D peak or G peak that would arise in this region, this peak can be assigned to amorphous carbon arising from the degradation of the polytetrafluoroethylene (PTFE) stir bars during the etching reaction.[59,60]

Optical Properties. The optical properties of both MXenes were measured by UV−vis−NIR spectroscopy and Fourier transform infrared spectroscopy (FTIR). The UV−vis−NIR spectrophotometry was performed on a serially diluted MXene solution after delamination, which allowed for the calculation of the extinction coefficient from Beer's law (Table S8). Neither MXene showed distinct peaks in the UV or NIR ranges, indicating a low optical activity in these ranges. Visually, the MXene solutions were both black (Figure S25). At 550 nm, the extinction coefficient (ε_{550}) was determined to be 18.7 L g^{-1} cm^{-1} for $Ti_{2.5}Ta_{2.5}C_4$ and 20.9 L g^{-1}cm^{-1} for $Ti_{2.675}Nb_{2.325}C_4$, both lower than the ε_{550} reported for Mo_4VC_4 of 34.4 L g^{-1}cm^{-1}, making these the lowest recorded extinction coefficient for any MXene.[8,36] To further explore the optical properties, FTIR measurements were performed on spray-coated films from the same single-flake solution (Figure 6; see Figure 2 for optical images of the spray-coated films). The MXene samples were then characterized using a Bruker Invenio FTIR spectrometer in total reflectance mode to investigate their emissivity, which is important for assessing IR shielding performance. The results reveal that the emissivity of both $Ti_{2.675}Nb_{2.325}C_4$ and $Ti_{2.5}Ta_{2.5}C_4$ MXenes is significantly higher than that of the reference Ti_3C_2 MXene sample (with reflectance being respectively significantly lower). $Ti_{2.675}Nb_{2.325}C_4$ showed slightly higher emissivity (and respectively lower in reflectivity) than $Ti_{2.5}Ta_{2.5}C_4$, indicating that the increase in atomic thickness and the addition of Nb and Ta in the MXene composition can lead to significant changes in their IR shielding properties. The IR shielding performance of M_5X_4 MXenes can be attributed to their electronic and structural properties. Further investigations are warranted to explore the full potential of M_5X_4 MXenes within IR shielding applications.

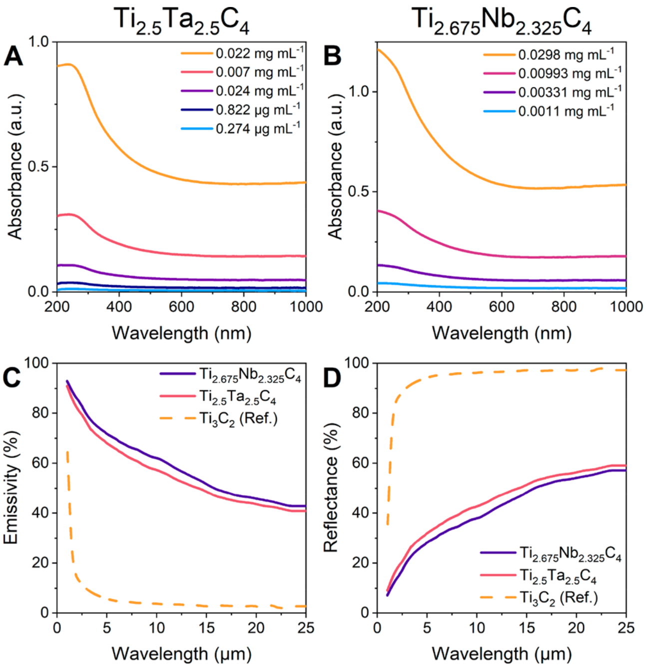

Figure 6. (A, B) UV−vis−NIR spectra of (A) $Ti_{2.5}Ta_{2.5}C_4$ and (B) $Ti_{2.675}Nb_{2.325}C_4$ MXene flakes in water, which were used to calculate the extinction coefficients. (C, D) FTIR spectra of spray-coated $Ti_{2.5}Ta_{2.5}C_4$ and $Ti_{2.675}Nb_{2.325}C_4$ films showing (C) emissivity and (D) reflectance compared to those of a Ti_3C_2 spray-coated reference film.

Thermal Stability. To investigate the thermal stability of both MAX-phase and multilayer MXene powders, thermogravimetric analysis (TGA) (Figure 7) coupled with residual gas analysis (RGA) was conducted (Figure S28). Both M_5AX_4 MAX phases show similar thermal stability to stoichiometric Ti_3AlC_2 MAX with the onset of oxidation under air at ~600 °C.[61] Further analysis of the weight gain, based on the large difference in molecular weight of Ti and Ta, also suggests that $Ti_{2.5}Ta_{2.5}AlC_4$ MAX contains little oxygen substitution in the carbon lattice (discussed in the Supporting Information). We speculate that the presence of a small amount of oxide is necessary to nucleate the formation of the MAX phases, where oxygen is present in the carbon lattice initially and helps stabilize the structure.

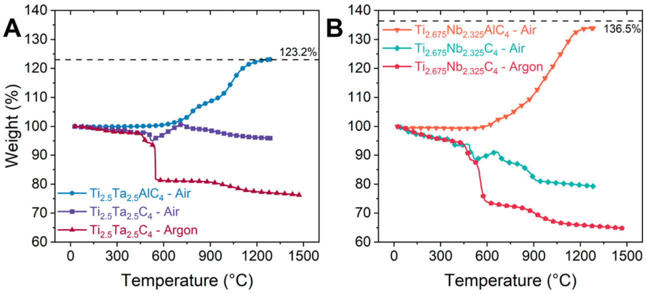

Figure 7. Thermogravimetric analysis of (A) $Ti_{2.5}Ta_{2.5}C_4$ and (B) $Ti_{2.675}Nb_{2.325}C_4$ MAX and MXenes under air and argon. The dashed line indicates the theoretical weight gain for MAX under air.

Thicker MXene sheets with more atomic layers are expected to be more thermally stable because their structures are closer to those of cubic carbides with a greater number of strong M−X bonds. However, compared to Ti_3C_2, both M_5X_4 MXenes do not show improved stability and instead show decomposition starting at ~450 °C under both inert and oxidizing atmospheres. Under air, two processes occur simultaneously: weight gain from oxidation of the metal and weight loss from pyrolysis of the carbon (Figure S28). Thus, a greater total weight loss from $Ti_{2.675}Nb_{2.325}C_4$ indicates that this sample is likely more defective than $Ti_{2.5}Ta_{2.5}C_4$. TEM analysis indicates that both samples contain point defects resulting from overetching due to the harsh etching conditions (long time, high temperature, and high HF concentration) (Figure S23F). XPS analysis indicates that the Ti in the $Ti_{2.675}Nb_{2.325}C_4$ sample is more oxidized than the Ti in $Ti_{2.5}Ta_{2.5}C_4$, and there is a greater amount of adventitious carbon, which indicates that the $Ti_{2.675}Nb_{2.325}C_4$ is more defective. Moreover, $Ti_{2.675}Nb_{2.325}C_4$ exhibits a higher weight loss from chemisorbed water (up to ~300 °C) with a first signature of CO_2 at a lower temperature (~225 °C) compared to $Ti_{2.5}Ta_{2.5}C_4$, which indicates a more defective MXene (Figures S27, S28). Considering that the final transition under an inert atmosphere occurs at ~900 °C for both MXenes, the thermal stability of nondefective M_5X_4 MXenes may indeed be higher than atomically thinner MXene structures. However, further improvements in the synthesis process are necessary to confirm this.

DFT Calculations. Following the discovery of $Ti_{2.5}Ta_{2.5}AlC_4$ and $Ti_{2.675}Nb_{2.325}AlC_4$, we used DFT to search for other stable M_5AX_4 MAX phases. To predict the stability for $(M'_{1-y}M''_y)_5AlC_4$ systems, two different crystal structures were considered: (i) the traditional MAX-phase structure (space group $P6_3/mmc$) and (ii) the recently reported twinned structure (space group $P\bar{6}m2$).[36] For each crystal structure, we have considered M′ and M″ in a random arrangement to mimic solid-solution disorder and with out-of-plane chemical order. The ordered arrangements considered are illustrated in Figure 8. For each composition, we solve the linear optimization problem, identify the equilibrium simplex, and

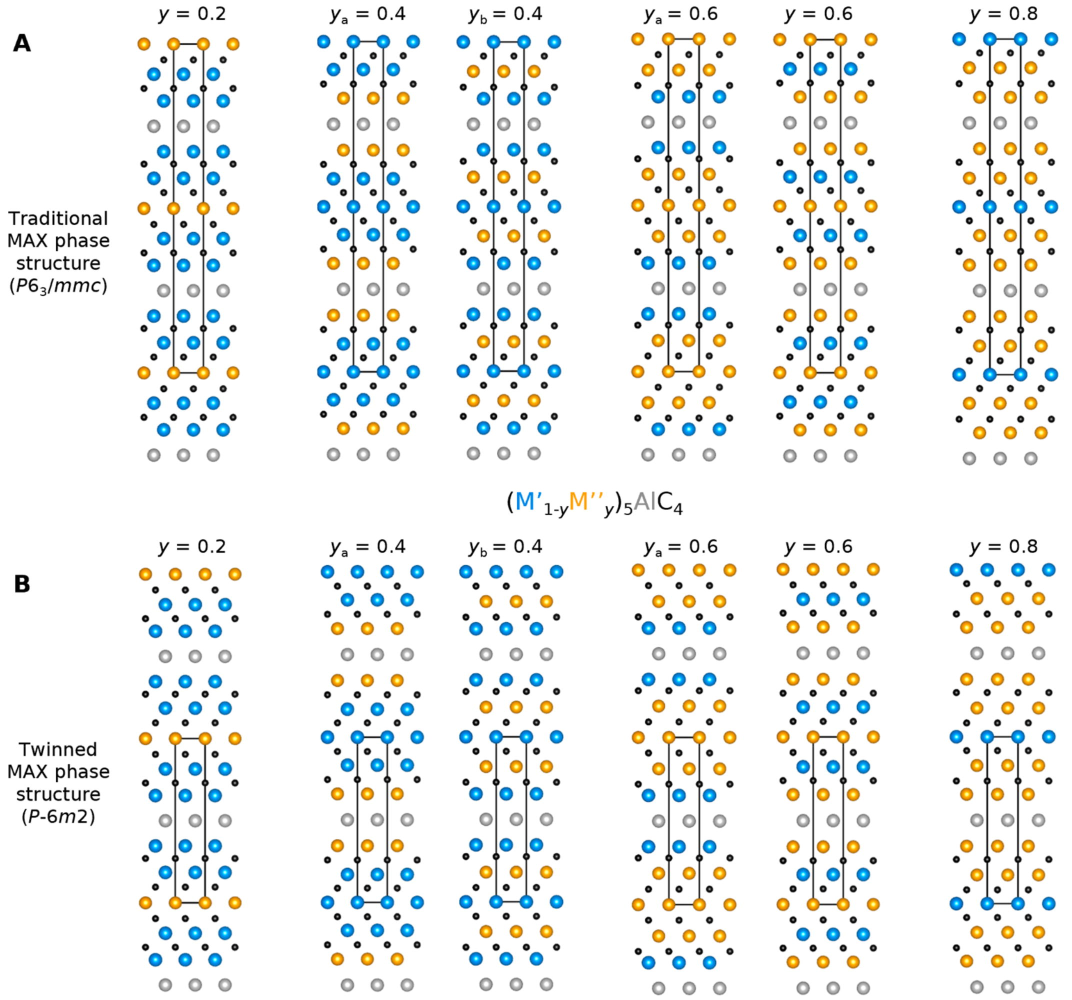

Figure 8. Schematic illustration of ordered arrangements considered for $(M'_{1-y}M''_y)_5AlC_4$ systems using (a) the traditional MAX-phase structure with space group $P6_3/mmc$ and (b) a twinned structure with space group $P\bar{6}m2$. M′ atoms are shown in blue, M″ in orange, Al in gray, and C in black.

calculate the stability ΔG_{cp} (eq 1). Note that all phases that have been modeled with solid-solution disorder, $(M'_{1-y}M''_y)_5AlC_4$ as well as competing phases including $(M'_{1-y}M''_y)_{n+1}AlC_n$ with n = 1, 2, and 3, have a contribution from configurational entropy to their Gibbs free energy (eqs 2 and 3).

Figure 9 shows the calculated Gibbs free energy of formation (estimated at 2000 K) for 10 different $(M'_{1-y}M''_y)_5AlC_4$ systems. Five of these systems (TiV, TiNb, TiTa, TaV, ScMo) have compositions predicted to be stable, with $\Delta G_{cp} < 0$, while the others are identified as closely stable with $0 \leq \Delta G_{cp} \leq 50$. Solid-solution disorder with the $P6_3/mmc$ structure is predicted to be stable for $(Ti_{0.4}V_{0.6})_5AlC_4$ in Figure 9A, $(Ti_{1-y}Nb_y)_5AlC_4$ in Figure 9B ($0.4 \leq y \leq 0.8$), $(Ti_{1-y}Ta_y)_5AlC_4$ in Figure 9E ($0.2 \leq y \leq 0.8$), and $(Sc_{1-y}Mo_y)_5AlC_4$ in Figure 9J ($0.4 \leq y \leq 0.6$). In some of these systems, the twinned $P\bar{6}m2$ structure is also found to be stable, but less so than the traditional MAX-phase structure. Focusing on the solid-solution disordered arrangements, the $P6_3/mmc$ structure is mostly lower in energy than $P\bar{6}m2$. However, $P\bar{6}m2$ is found to be more favored in Mo-based systems as shown in Figure 9D,G−I.

Solid-solution disorder is typically lower in energy than herein considered ordered arrangements. However, in Mo-based systems, it is found that chemical order is favored, as seen in Figure 9D,G−J. Out of these ordered structures, three are predicted to be stable: one in the $P6_3/mmc$ structure, $Mo_3Sc_2AlC_4$ (y_b = 0.6 in Figure 9J), and two in the twinned $P\bar{6}m2$ structure, $Mo_3Ti_2AlC_4$ and $Mo_3Sc_2AlC_4$ (y_b = 0.6 in Figure 9H,J). Other ordered Mo-based structures are found close to stable, i.e., with $0 \leq \Delta G_{cp} \leq 50$. It should be noted that all three stable phases have an ordered arrangement where Mo is located both in the middle layer and next to the Al layer. This arrangement is marked with y_b = 0.6 in Figure 9. Furthermore, we have considered ideal structures with M-, A-, and X-sites being fully occupied; that is, no vacancies have been considered. The impact of defects, such as vacancies, may stabilize these phases further. Any deviation in the theoretical stability predictions and the experimentally derived MAX phases may be due to the addition of oxides during synthesis.

CONCLUSION

The successful syntheses of $Ti_{2.5}Ta_{2.5}C_4$ and $Ti_{2.675}Nb_{2.325}C_4$ establish the M_5X_4 family beyond Mo_4VC_4. $Ti_{2.5}Ta_{2.5}C_4$ and $Ti_{2.675}Nb_{2.325}C_4$ were both confirmed to be disordered solid solutions on the M-site, and $Ti_{2.5}Ta_{2.5}C_4$ was confirmed to exhibit the same twinned structure found in Mo_4VC_4, indicating this structure may be a hallmark of the M_5X_4

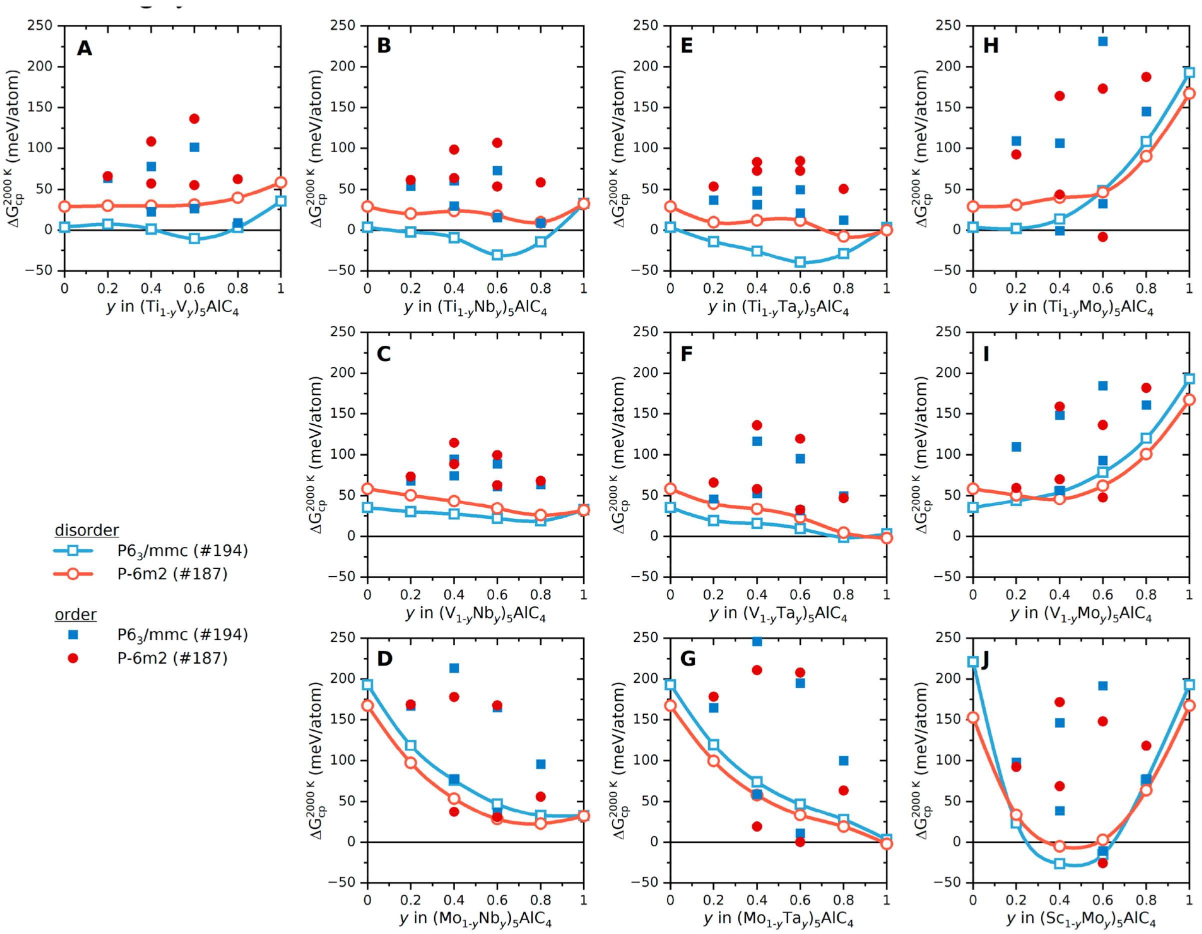

Figure 9. Calculated stability at 2000 K, $\Delta G_{cp}^{2000\ K}$, for different quaternary $(M'_{1-y}M''_y)_5AlC_4$ as a function of *x* assuming the traditional MAX-phase structure with space group $P6_3/mmc$ (blue squares) or a twinned structure with space group $P\bar{6}m2$ (red circles). The distributions of M′ and M″ on the M-sites have been considered with a random arrangement to mimic solid-solution disorder (filled symbols) and as out-of-plane order (open symbols).

family. The studied MXenes demonstrate exciting thermal and optical properties not found in other MXenes, making them a promising candidate for optoelectronics, electrochemical, and high-temperature applications. The successful use of DFT predictions to isolate stable MAX phases has the possibility of mapping other favorable M_5AX_4 MAX phases to further expand the MXene family. These reported MAX phases and MXenes comprise an established M_5X_4 family that can be successfully synthesized and isolated to be phase-pure.

EXPERIMENTAL SECTION

Synthesis of $Ti_{2.5}Ta_{2.5}AlC_4$ and $Ti_{2.675}Nb_{2.325}C_4$ MAX Phases. Titanium (∼325 mesh, 99.5% metals basis), titanium(IV) oxide, niobium (∼325 mesh, 99.8% metals basis), niobium(V) oxide (99.5% metals basis), tantalum (∼325 mesh, 99.9% metals basis, 99.6%), tantalum(V) oxide (99% metals basis), molybdenum (∼250 mesh, 99.9% metals basis), molybdenum(VI) oxide (99.5%), vanadium (∼325 mesh, 99.5%), vanadium(V) oxide (99.2%), aluminum (∼325 mesh, 99.5% (metals basis)), and graphite (∼325 mesh, 99%) powders were combined in varying atomic ratios (see Supporting Information) and ball-milled at 70 rpm for 12 h at a ratio of 1:2 = powder:yttria-stabilized zirconia (YSZ) balls by weight. The mixtures were then heated in alumina crucibles at 3 °C min^{-1} to 1650 °C under 350 cm^3 min^{-1} flowing argon in a tube furnace (Carbolite Gero) and held for 24 h before cooling to room temperature, also at 3 °C min^{-1}. The sintered materials were then ground to powder using a mortar and pestle. The resulting MAX phases were stirred in 9 M hydrochloric acid for 12 h to dissolve intermetallic impurities, then washed to neutral pH by vacuum filtration with water. The powders were collected and dried overnight at room temperature under vacuum. The powders were then sieved using stainless-steel meshes to obtain a particle size of <75 μm for uniform etching.

Synthesis of $Ti_{2.5}Ta_{2.5}C_4$ and $Ti_{2.675}Nb_{2.325}C_4$ MXenes. To synthesize multilayer MXenes, 6 g of MAX powders was slowly added to 60 mL of HF (48−51% Acros Organics) while being stirred with a PTFE-coated stir bar at 400 rpm. For the synthesis of $Ti_{2.5}Ta_{2.5}C_4$, the reaction was carried out for 9 days, while for the synthesis of $Ti_{2.675}Nb_{2.325}C_4$, the reaction was carried out for 7 days. Both reactions were held at 50 °C in a mineral oil bath. After completion, the samples were washed via a series of cycles involving centrifugation at 3500 rpm (2550 rcf) for 10 min, decanting the acidic supernatant, and redispersion of the sediment using deionized (DI) water until the supernatant reached a neutral pH. The multilayer MXene powder was then collected by vacuum-assisted filtration through a porous membrane (MF-Millipore 0.45 μm mixed cellulose ester).

To produce delaminated MXene flakes, 1 g of multilayer $Ti_{2.5}Ta_{2.5}C_4$ or $Ti_{2.675}Nb_{2.325}C_4$ MXene powders was dispersed in 20 mL of 5 wt % tetramethylammonium hydroxide (TMAOH, 25 wt %, diluted to 5 wt %, Sigma-Aldrich) and stirred at 400 rpm for 24 h at 35 °C. TMAOH was then washed out through a series of cycles involving centrifugation at 10,000 rpm (12,850 rcf) for 10 min, discarding the supernatant, and redispersing the sediment with DI water. A paint shaker was used to redisperse the sediment because it adhered strongly to the walls of the centrifuge tube. This process was repeated until the supernatant had a pH < 8. From here, the sediment was redispersed in DI water, shaken for 30 min, then centrifuged at

3500 rpm (2550 rcf) for 30 min. The resulting black supernatant was carefully decanted to collect the delaminated MXene. This process was repeated twice to collect approximately 300 mL of MXene. The concentration of the single-flake solution was determined by drop-casting 100 μL of the solution onto oven-dried silicon wafers, drying, and measuring the weight change.

Film Preparation. To obtain free-standing films, the delaminated MXene flake colloid was filtered via vacuum-assisted filtration through a porous membrane (Celgard 3501, 64 nm pore size, polypropylene). The resulting films were separated from the Celgard and stored in a vacuum desiccator at room temperature.

Structural Characterization. The crystal structures of all powders were characterized by XRD. Rigaku SmartLab (40 kV/30 mA) and MiniFlex (40 kV/15 mA) X-ray diffractometers were used with Ni-filtered Cu Kα radiation. The step size of the scan was 0.01°, with a step duration of 4 s for MAX-phase powders and 2 s for the multilayer MXene powders and films.

The flake size and zeta potential were determined with a Malvern Zetasizer NanoZS DLS instrument, using a disposable capillary cell. Three measurements were taken per sample and averaged for the final flake size.

Microscopy. SEM micrographs were obtained with a Zeiss Supra 50VP scanning electron microscope. Transmission electron microscopy (TEM), scanning transmission electron microscopy (STEM), selected area electron diffraction (SAED), and energy dispersive spectroscopy (EDS) were performed on a JEOL 2100F FEG microscope operating at 200 kV. Samples were prepared from colloids containing the MAX-phase powders, and MXene powders/flakes were drop-cast onto lacy carbon copper grids. AFM was performed on drop-cast MXene flakes on silicon wafers with a dioxide layer using a Bruker Multimode 8 with a Si tip (Budget Sensors Tap300Al-G; $f_0 = 300$ kHz, $k = 40$ N m^{-1}) in tapping mode in air.

Chemical Composition. X-ray photoelectron spectra were collected by using a spectrometer (Versa Probe 5000, Physical Electronics) equipped with a monochromatic Al Kα X-ray source with a 200 μm spot size. Charge neutralization was performed by using a dual-beam setup supplying low-energy electrons and Ar$^+$ ions. High-resolution spectra were collected at a pass energy of 23.5 eV with a step size of 0.05 eV, whereas the survey spectra were collected at a pass energy of 117 eV with a step size of 0.5 eV. The quantification and curve fitting of the core-level spectra were performed using the Casa XPS software package with Shirley-type backgrounds. The carbon−metal component at 282.0 eV in the C 1s spectra was used for the binding energy scale correction.

Raman spectra were obtained using an inverted reflection mode spectrometer (Renishaw inVia) with a 63× (NA = 0.7) objective, diffraction-based room-temperature detector, and 633 nm laser with an 1800 line/mm grating. The laser power was in the ∼0.5−1 mW range.

Optical Properties. UV−vis−NIR spectra were collected by using a Thermo Scientific Evolution 201 spectrometer in transmission mode from 200 to 1000 nm. Samples were prepared by serial dilution of delaminated MXene solutions with DI water and measured in quartz cuvettes (1 cm path length and water for blank measurement). The extinction was normalized to path length and plotted against concentration to find the extinction coefficient according to the Beer−Lambert equation ($A = \varepsilon bC$). FTIR spectra were obtained by using spray-coated MXene films on glass substrates. Surface roughness of the MXene films was obtained using an optical profiler (Keyence VK-X1050 with a 785 nm laser).

The FTIR measurements were performed using a Bruker Invenio spectrometer in total reflectance mode. The resolution was set to 4 cm^{-1} with 14 scans total, and the Opus software was used to apply smoothing with 5 points average. Measurements were taken at room temperature and average humidity. Gold-coated mirror was used as a reference background, and the background was respectively subtracted for each sample in the 1 to 25 μm range.

Thermal Analysis. The high-temperature behavior of MAX-phase and multilayer MXene powders was studied using thermogravimetric analysis (SDT 650, TA Instruments) coupled to evolved gas analysis (Discovery mass spectrometer, TA Instruments). Powders with masses around 15 mg were packed in a 90 μL alumina pan and heated to 1300 °C (under 100 mL min^{-1} dry airflow) or 1500 °C (under 300 mL min^{-1} Ar flow) at 20 °C min^{-1}.

DFT Calculations. All first-principles calculations were performed by means of DFT and the projector augmented wave method,[62,63] as implemented within the Vienna ab initio simulation package (VASP) version 5.4.1.[64−66] We used the non-spin-polarized generalized gradient approximation (GGA) as parametrized by Perdew−Burke−Ernzerhof (PBE) for treating the electron exchange and correlation effects.[67]

To model chemical disorder of M′ and M″ on the M sublattice for $(\mathrm{M}'_{1-y}\mathrm{M}''_{y})_{n+1}\mathrm{AlC}_n$ with $n = 1$ to 4, we used the special quasi-random structure (SQS) method[68] to generate supercells composed of 72 to 256 atoms. Convergency tests in previous works show that the supercells used give a qualitatively accurate representation and a quantitative convergency in terms of calculated formation enthalpies and lattice parameters.[69,70]

The thermodynamic stability of the quaternary MAX phases was investigated at 2000 K with respect to decomposition into any combination of competing phases. The set of most competing phases, denoted equilibrium simplex, is identified using a linear optimization procedure[71,72] which has been proven successful in confirming already experimentally known MAX phases as well as predicting the existence of new ones.[19,50,69,70,72−76] The stability of the quaternary MAX phase is quantified in terms of the formation Gibbs free energy ΔG_{cp} by comparing its energy to the energy of the equilibrium simplex using

$$\Delta G_{\mathrm{cp}} = G((M'_{1-y}M''_{y})_5\mathrm{AlC}_4) - G\ (\text{equilibrium simplex}) \tag{1}$$

A phase is concluded to be stable when $\Delta G_{\mathrm{cp}} < 0$ or at best metastable for $\Delta G_{\mathrm{cp}} > 0$. Note that since we evaluate the stability at 2000 K, configurational entropy will decrease the Gibbs free energy if the phase is considered to have a solid solution disorder. This is the case both for $(\mathrm{M}'_{1-y}\mathrm{M}''_{y})_5\mathrm{AlC}_4$ and for competing phases like lower-order MAX phases $(\mathrm{M}'_{1-y}\mathrm{M}''_{y})_2\mathrm{AlC}$, $(\mathrm{M}'_{1-y}\mathrm{M}''_{y})_3\mathrm{AlC}_2$, and $(\mathrm{M}'_{1-y}\mathrm{M}''_{y})_4\mathrm{AlC}_3$. The contribution from configurational entropy due to the disorder of M′ and M″ on the M sublattices will decrease the Gibbs free energy G^{disorder} as approximated by

$$G^{\mathrm{disorder}}[T] = H^{\mathrm{disorder}} - T\Delta S \tag{2}$$

where the entropic contribution ΔS, assuming an ideal solution of M′ and M″ on the M-sites, is given by

$$\Delta S = -k_{\mathrm{B}}[y\ \ln(y) + (1 - y)\ln(1 - y)] \tag{3}$$

where k_{B} is the Boltzmann constant and y is the concentration of M′ on the M-sublattice.

ASSOCIATED CONTENT

Supporting Information

The Supporting Information is available free of charge at https://pubs.acs.org/doi/10.1021/acsnano.3c04967.

> Additional powder XRDs of the other ratios used in the composition search for other M_5AX_4 MAX phases; details of the synthesis procedure for the M_5AX_4 MAX phases and MXenes including synthesis optimization details; DLS flake size and zeta potential; AFM of flake thickness; TEM of $\mathrm{Ti}_{2.5}\mathrm{Ta}_{2.5}\mathrm{AlC}_4$ MAX phase and MXene; EDS of both reported MAX phases and MXenes; XPS results; UV−vis−NIR spectroscopy analysis; extended Raman spectroscopy; thermal analysis DTA and mass spectroscopy; and Rietveld refinement of the M_5AX_4 MAX-phase powder XRDs (PDF)

AUTHOR INFORMATION

Corresponding Author

Yury Gogotsi − *Department of Materials Science and Engineering and A.J. Drexel Nanomaterials Institute, Drexel University, Philadelphia, Pennsylvania 19104, United States;* orcid.org/0000-0001-9423-4032; Email: gogotsi@drexel.edu

Authors

Marley Downes − *Department of Materials Science and Engineering and A.J. Drexel Nanomaterials Institute, Drexel University, Philadelphia, Pennsylvania 19104, United States;* orcid.org/0009-0007-4436-7305

Christopher E. Shuck − *Department of Materials Science and Engineering and A.J. Drexel Nanomaterials Institute, Drexel University, Philadelphia, Pennsylvania 19104, United States;* orcid.org/0000-0002-1274-8484

Robert W. Lord − *Department of Materials Science and Engineering and A.J. Drexel Nanomaterials Institute, Drexel University, Philadelphia, Pennsylvania 19104, United States*

Mark Anayee − *Department of Materials Science and Engineering and A.J. Drexel Nanomaterials Institute, Drexel University, Philadelphia, Pennsylvania 19104, United States;* orcid.org/0000-0002-6691-920X

Mikhail Shekhirev − *Department of Materials Science and Engineering and A.J. Drexel Nanomaterials Institute, Drexel University, Philadelphia, Pennsylvania 19104, United States;* orcid.org/0000-0002-8381-1276

Ruocun John Wang − *Department of Materials Science and Engineering and A.J. Drexel Nanomaterials Institute, Drexel University, Philadelphia, Pennsylvania 19104, United States;* orcid.org/0000-0001-8095-5285

Tetiana Hryhorchuk − *Department of Materials Science and Engineering and A.J. Drexel Nanomaterials Institute, Drexel University, Philadelphia, Pennsylvania 19104, United States*

Martin Dahlqvist − *Materials Design Division, Department of Physics, Chemistry and Biology (IFM), Linköping University, SE-581 83 Linköping, Sweden;* orcid.org/0000-0001-5036-2833

Johanna Rosen − *Materials Design Division, Department of Physics, Chemistry and Biology (IFM), Linköping University, SE-581 83 Linköping, Sweden;* orcid.org/0000-0002-5173-6726

Complete contact information is available at:
https://pubs.acs.org/10.1021/acsnano.3c04967

Notes

The authors declare no competing financial interest.

Marley Downes, Christopher E. Shuck, Robert W. Lord, Mark Anayee, Mikhail Shekhirev, Ruocun (John) Wang, Tetiana Hryhorchuk, Martin Dahlqvist, Johanna Rosen, Yury Gogotsi. M_5X_4 − A Family of MXenes. 2023, Version 1. ChemRxiv. https://chemrxiv.org/engage/chemrxiv/article-details/648b2daabe16ad5c57f865e4 (accessed August 8, 2023).

ACKNOWLEDGMENTS

The authors would like to acknowledge the U.S. National Science Foundation, Grant DMR-2041050, for funding this project. M.D. thanks Murata Manufacturing, Japan, and the Drexel UREP Undergraduate Research Grant for their support in funding her undergraduate research. M.A. was supported by the U.S. Department of Education Graduate Assistance in Areas of National Need (GAANN) fellowship. J.R. acknowledges funding from the Swedish Research Council, no. 2019-04233. The authors would also like to acknowledge the usage of the XRD, XPS, SEM, and TEM/EDS instrumentation provided by the Drexel University Materials Characterization Core (MCC). Collaboration between Drexel University and Linkoping University was supported by The Wallenberg Initiative Materials Science for Sustainability (WISE). The calculations were enabled by resources provided by the National Academic Infrastructure for Supercomputing in Sweden (NAISS) and the Swedish National Infrastructure for Computing (SNIC) at the National Supercomputer Center (NSC) partially funded by the Swedish Research Council through grant agreements no. 2022-06725 and no. 2018-05973.

REFERENCES

(1) Naguib, M.; Kurtoglu, M.; Presser, V.; Lu, J.; Niu, J.; Heon, M.; Hultman, L.; Gogotsi, Y.; Barsoum, M. W. Two-Dimensional Nanocrystals Produced by Exfoliation of Ti_3AlC_2. *Adv. Mater.* **2011**, *23* (37), 4248−4253.

(2) Anasori, B.; Naguib, M. Two-Dimensional MXenes *MRS Bull.* **2023**, *48* (3), 238−244. .

(3) Kamysbayev, V.; Filatov, A. S.; Hu, H.; Rui, X.; Lagunas, F.; Wang, D.; Klie, R. F.; Talapin, D. V. Covalent Surface Modifications and Superconductivity of Two-Dimensional Metal Carbide MXenes. *Science* **2020**, *369* (6506), 979−983.

(4) Zhang, C. J.; Anasori, B.; Seral-Ascaso, A.; Park, S.-H.; McEvoy, N.; Shmeliov, A.; Duesberg, G. S.; Coleman, J. N.; Gogotsi, Y.; Nicolosi, V. Transparent, Flexible, and Conductive 2D Titanium Carbide (MXene) Films with High Volumetric Capacitance. *Adv. Mater.* **2017**, *29* (36), No. 1702678.

(5) Han, M.; Maleski, K.; Shuck, C. E.; Yang, Y.; Glazar, J. T.; Foucher, A. C.; Hantanasirisakul, K.; Sarycheva, A.; Frey, N. C.; May, S. J.; Shenoy, V. B.; Stach, E. A.; Gogotsi, Y. Tailoring Electronic and Optical Properties of MXenes through Forming Solid Solutions. *J. Am. Chem. Soc.* **2020**, *142* (45), 19110−19118.

(6) Jastrzębska, A. M.; Szuplewska, A.; Wojciechowski, T.; Chudy, M.; Ziemkowska, W.; Chlubny, L.; Rozmysłowska, A.; Olszyna, A. In Vitro Studies on Cytotoxicity of Delaminated Ti_3C_2 MXene. *J. Hazard. Mater.* **2017**, *339*, 1−8.

(7) Hantanasirisakul, K.; Zhao, M.-Q.; Urbankowski, P.; Halim, J.; Anasori, B.; Kota, S.; Ren, C. E.; Barsoum, M. W.; Gogotsi, Y. Fabrication of $Ti_3C_2T_x$ MXene Transparent Thin Films with Tunable Optoelectronic Properties. *Adv. Electron. Mater.* **2016**, *2* (6), 1600050.

(8) Maleski, K.; Shuck, C. E.; Fafarman, A. T.; Gogotsi, Y. The Broad Chromatic Range of Two-Dimensional Transition Metal Carbides. *Adv. Opt. Mater.* **2021**, *9* (4), No. 2001563.

(9) Li, X.; Huang, Z.; Shuck, C. E.; Liang, G.; Gogotsi, Y.; Zhi, C. MXene Chemistry, Electrochemistry and Energy Storage Applications. *Nat. Rev. Chem.* **2022**, *6* (6), 389−404.

(10) Li, H.; Fan, R.; Zou, B.; Yan, J.; Shi, Q.; Guo, G. Roles of MXenes in Biomedical Applications: Recent Developments and Prospects. *J. Nanobiotechnology* **2023**, *21* (1), 73.

(11) Zhang, D.; Shah, D.; Boltasseva, A.; Gogotsi, Y. MXenes for Photonics. *ACS Photonics* **2022**, *9* (4), 1108−1116.

(12) Iqbal, A.; Sambyal, P.; Koo, C. M. 2D MXenes for Electromagnetic Shielding: A Review. *Adv. Funct. Mater.* **2020**, *30* (47), 2000883.

(13) VahidMohammadi, A.; Rosen, J.; Gogotsi, Y. The World of Two-Dimensional Carbides and Nitrides (MXenes). *Science* **2021**, *372* (6547), No. eabf1581.

(14) Lim, K. R. G.; Shekhirev, M.; Wyatt, B. C.; Anasori, B.; Gogotsi, Y.; Seh, Z. W. Fundamentals of MXene Synthesis. *Nat. Synth.* **2022**, *1* (8), 601−614.

(15) Mashtalir, O.; Naguib, M.; Mochalin, V. N.; Dall'Agnese, Y.; Heon, M.; Barsoum, M. W.; Gogotsi, Y. Intercalation and

Delamination of Layered Carbides and Carbonitrides. *Nat. Commun.* **2013**, *4* (1), 1716.

(16) Naguib, M.; Unocic, R. R.; Armstrong, B. L.; Nanda, J. Large-Scale Delamination of Multi-Layers Transition Metal Carbides and Carbonitrides "MXenes. *Dalton Trans.* **2015**, *44* (20), 9353−9358.

(17) Wang, D.; Zhou, C.; Filatov, A. S.; Cho, W.; Lagunas, F.; Wang, M.; Vaikuntanathan, S.; Liu, C.; Klie, R. F.; Talapin, D. V. Direct Synthesis and Chemical Vapor Deposition of 2D Carbide and Nitride MXenes. *Science* **2023**, *379* (6638), 1242−1247.

(18) Naguib, M.; Halim, J.; Lu, J.; Cook, K. M.; Hultman, L.; Gogotsi, Y.; Barsoum, M. W. New Two-Dimensional Niobium and Vanadium Carbides as Promising Materials for Li-Ion Batteries. *J. Am. Chem. Soc.* **2013**, *135* (43), 15966−15969.

(19) Tao, Q.; Dahlqvist, M.; Lu, J.; Kota, S.; Meshkian, R.; Halim, J.; Palisaitis, J.; Hultman, L.; Barsoum, M. W.; Persson, P. O. Å.; Rosen, J. Two-Dimensional $Mo_{1.33}C$ MXene with Divacancy Ordering Prepared from Parent 3D Laminate with in-Plane Chemical Ordering. *Nat. Commun.* **2017**, *8* (1), No. 14949.

(20) Soundiraraju, B.; George, B. K. Two-Dimensional Titanium Nitride (Ti_2N) MXene: Synthesis, Characterization, and Potential Application as Surface-Enhanced Raman Scattering Substrate. *ACS Nano* **2017**, *11* (9), 8892−8900.

(21) Urbankowski, P.; Anasori, B.; Hantanasirisakul, K.; Yang, L.; Zhang, L.; Haines, B.; May, S. J.; Billinge, S. J. L.; Gogotsi, Y. 2D Molybdenum and Vanadium Nitrides Synthesized by Ammoniation of 2D Transition Metal Carbides (MXenes). *Nanoscale* **2017**, *9* (45), 17722−17730.

(22) Meshkian, R.; Näslund, L.-Å.; Halim, J.; Lu, J.; Barsoum, M. W.; Rosen, J. Synthesis of Two-Dimensional Molybdenum Carbide, Mo_2C, from the Gallium Based Atomic Laminate Mo_2Ga_2C. *Scr. Mater.* **2015**, *108*, 147−150.

(23) Meshkian, R.; Dahlqvist, M.; Lu, J.; Wickman, B.; Halim, J.; Thörnberg, J.; Tao, Q.; Li, S.; Intikhab, S.; Snyder, J.; Barsoum, M. W.; Yildizhan, M.; Palisaitis, J.; Hultman, L.; Persson, P. O. Å.; Rosen, J. W-Based Atomic Laminates and Their 2D Derivative $W_{1.33}C$ MXene with Vacancy Ordering. *Adv. Mater.* **2018**, *30* (21), No. 1706409.

(24) Persson, I.; el Ghazaly, A.; Tao, Q.; Halim, J.; Kota, S.; Darakchieva, V.; Palisaitis, J.; Barsoum, M. W.; Rosen, J.; Persson, P. O. Å. Tailoring Structure, Composition, and Energy Storage Properties of MXenes from Selective Etching of In-Plane, Chemically Ordered MAX Phases. *Small* **2018**, *14* (17), No. 1703676.

(25) Halim, J.; Palisaitis, J.; Lu, J.; Thörnberg, J.; Moon, E. J.; Precner, M.; Eklund, P.; Persson, P. O. Å.; Barsoum, M. W.; Rosen, J. Synthesis of Two-Dimensional $Nb_{1.33}C$ (MXene) with Randomly Distributed Vacancies by Etching of the Quaternary Solid Solution $(Nb_{2/3}Sc_{1/3})_2AlC$ MAX Phase. *ACS Appl. Nano Mater.* **2018**, *1* (6), 2455−2460.

(26) Anasori, B.; Gogotsi, Y. MXenes: Trends, Growth, and Future Directions. *Graphene 2D Mater.* **2022**, *7* (3), 75−79.

(27) Naguib, M.; Mashtalir, O.; Carle, J.; Presser, V.; Lu, J.; Hultman, L.; Gogotsi, Y.; Barsoum, M. W. Two-Dimensional Transition Metal Carbides. *ACS Nano* **2012**, *6* (2), 1322−1331.

(28) Zhou, J.; Zha, X.; Zhou, X.; Chen, F.; Gao, G.; Wang, S.; Shen, C.; Chen, T.; Zhi, C.; Eklund, P.; Du, S.; Xue, J.; Shi, W.; Chai, Z.; Huang, Q. Synthesis and Electrochemical Properties of Two-Dimensional Hafnium Carbide. *ACS Nano* **2017**, *11* (4), 3841−3850.

(29) Zhou, J.; Zha, X.; Chen, F. Y.; Ye, Q.; Eklund, P.; Du, S.; Huang, Q. A Two-Dimensional Zirconium Carbide by Selective Etching of Al_3C_3 from Nanolaminated $Zr_3Al_3C_5$. *Angew. Chem., Int. Ed.* **2016**, *55* (16), 5008−5013.

(30) Anasori, B.; Xie, Y.; Beidaghi, M.; Lu, J.; Hosler, B. C.; Hultman, L.; Kent, P. R. C.; Gogotsi, Y.; Barsoum, M. W. Two-Dimensional, Ordered, Double Transition Metals Carbides (MXenes). *ACS Nano* **2015**, *9* (10), 9507−9516.

(31) Meshkian, R.; Tao, Q.; Dahlqvist, M.; Lu, J.; Hultman, L.; Rosen, J. Theoretical Stability and Materials Synthesis of a Chemically Ordered MAX Phase, Mo_2ScAlC_2, and Its Two-Dimensional Derivate Mo_2ScC_2 MXene. *Acta Mater.* **2017**, *125*, 476−480.

(32) Yang, J.; Naguib, M.; Ghidiu, M.; Pan, L.-M.; Gu, J.; Nanda, J.; Halim, J.; Gogotsi, Y.; Barsoum, M. W. Two-Dimensional Nb-Based M_4C_3 Solid Solutions (MXenes). *J. Am. Ceram. Soc.* **2016**, *99* (2), 660−666.

(33) Urbankowski, P.; Anasori, B.; Makaryan, T.; Er, D.; Kota, S.; Walsh, P. L.; Zhao, M.; Shenoy, V. B.; Barsoum, M. W.; Gogotsi, Y. Synthesis of Two-Dimensional Titanium Nitride Ti_4N_3 (MXene). *Nanoscale* **2016**, *8* (22), 11385−11391.

(34) Tran, M. H.; Schäfer, T.; Shahraei, A.; Dürrschnabel, M.; Molina-Luna, L.; Kramm, U. I.; Birkel, C. S. Adding a New Member to the MXene Family: Synthesis, Structure, and Electrocatalytic Activity for the Hydrogen Evolution Reaction of $V_4C_3T_x$. *ACS Appl. Energy Mater.* **2018**, *1* (8), 3908−3914.

(35) Ghidiu, M.; Naguib, M.; Shi, C.; Mashtalir, O.; Pan, L. M.; Zhang, B.; Yang, J.; Gogotsi, Y.; Billinge, S. J. L.; Barsoum, M. W. Synthesis and Characterization of Two-Dimensional Nb_4C_3 (MXene). *Chem. Commun.* **2014**, *50* (67), 9517−9520.

(36) Deysher, G.; Shuck, C. E.; Hantanasirisakul, K.; Frey, N. C.; Foucher, A. C.; Maleski, K.; Sarycheva, A.; Shenoy, V. B.; Stach, E. A.; Anasori, B.; Gogotsi, Y. Synthesis of Mo_4VAlC_4 MAX Phase and Two-Dimensional Mo_4VC_4 MXene with Five Atomic Layers of Transition Metals. *ACS Nano* **2020**, *14* (1), 204−217.

(37) Kurtoglu, M.; Naguib, M.; Gogotsi, Y.; Barsoum, M. W. First Principles Study of Two-Dimensional Early Transition Metal Carbides. *MRS Commun.* **2012**, *2* (4), 133−137.

(38) Tan, T. L.; Jin, H. M.; Sullivan, M. B.; Anasori, B.; Gogotsi, Y. High-Throughput Survey of Ordering Configurations in MXene Alloys Across Compositions and Temperatures. *ACS Nano* **2017**, *11* (5), 4407−4418.

(39) Ahmed, B.; Ghazaly, A. E.; Rosen, J. I-MXenes for Energy Storage and Catalysis. *Adv. Funct. Mater.* **2020**, *30* (47), No. 2000894.

(40) Hong, W.; Wyatt, B. C.; Nemani, S. K.; Anasori, B. Double Transition-Metal MXenes: Atomistic Design of Two-Dimensional Carbides and Nitrides. *MRS Bull.* **2020**, *45* (10), 850−861.

(41) Sun, W.; Wang, H.-W.; Vlcek, L.; Peng, J.; Brady, A. B.; Osti, N. C.; Mamontov, E.; Tyagi, M.; Nanda, J.; Greenbaum, S. G.; Kent, P. R. C.; Naguib, M. Multiscale and Multimodal Characterization of 2D Titanium Carbonitride MXene. *Adv. Mater. Interfaces* **2020**, *7* (11), No. 1902207.

(42) Pinto, D.; Anasori, B.; Avireddy, H.; Shuck, C. E.; Hantanasirisakul, K.; Deysher, G.; Morante, J. R.; Porzio, W.; Alshareef, H. N.; Gogotsi, Y. Synthesis and Electrochemical Properties of 2D Molybdenum Vanadium Carbides − Solid Solution MXenes. *J. Mater. Chem. A* **2020**, *8* (18), 8957−8968.

(43) Seredych, M.; Shuck, C. E.; Pinto, D.; Alhabeb, M.; Precetti, E.; Deysher, G.; Anasori, B.; Kurra, N.; Gogotsi, Y. High-Temperature Behavior and Surface Chemistry of Carbide MXenes Studied by Thermal Analysis. *Chem. Mater.* **2019**, *31* (9), 3324−3332.

(44) Shekhirev, M.; Shuck, C. E.; Sarycheva, A.; Gogotsi, Y. Characterization of MXenes at Every Step, from Their Precursors to Single Flakes and Assembled Films. *Prog. Mater. Sci.* **2021**, *120*, No. 100757.

(45) Hart, J. L.; Hantanasirisakul, K.; Lang, A. C.; Anasori, B.; Pinto, D.; Pivak, Y.; van Omme, J. T.; May, S. J.; Gogotsi, Y.; Taheri, M. L. Control of MXenes' Electronic Properties through Termination and Intercalation. *Nat. Commun.* **2019**, *10* (1), 522.

(46) Lipatov, A.; Lu, H.; Alhabeb, M.; Anasori, B.; Gruverman, A.; Gogotsi, Y.; Sinitskii, A. Elastic Properties of 2D $Ti_3C_2T_x$ MXene Monolayers and Bilayers. *Sci. Adv.* **2018**, *4* (6), No. eaat0491.

(47) Lipatov, A.; Alhabeb, M.; Lu, H.; Zhao, S.; Loes, M. J.; Vorobeva, N. S.; Dall'Agnese, Y.; Gao, Y.; Gruverman, A.; Gogotsi, Y.; Sinitskii, A. Electrical and Elastic Properties of Individual Single-Layer $Nb_4C_3T_x$ MXene Flakes. *Adv. Electron. Mater.* **2020**, *6* (4), No. 1901382.

(48) Liu, Y.; He, X.; Feng, J.; Wang, D.; Obeng, E.; Yu, C.; Song, Y.; Shen, J.; Li, Z. Engineering A New Member of MXenes M_5C_4 Phases Nanoplatforms as Synergistically Photothermal and Chemodynamic Therapeutics for Methicillin-Resistant Staphylococcus Aureus. *Chem. Eng. J.* **2023**, *466*, No. 143004.

(49) Zheng, L.; Wang, J.; Lu, X.; Li, F.; Wang, J.; Zhou, Y. $(Ti_{0.5}Nb_{0.5})_5AlC_4$: A New-Layered Compound Belonging to MAX Phases. *J. Am. Ceram. Soc.* **2010**, *93* (10), 3068−3071.

(50) Dahlqvist, M.; Lu, J.; Meshkian, R.; Tao, Q.; Hultman, L.; Rosen, J. Prediction and Synthesis of a Family of Atomic Laminate Phases with Kagomé-like and in-Plane Chemical Ordering. *Sci. Adv.* **2017**, *3* (7), No. e1700642.

(51) Michałowski, P. P.; Anayee, M.; Mathis, T. S.; Kozdra, S.; Wójcik, A.; Hantanasirisakul, K.; Jóźwik, I.; Piątkowska, A.; Możdżonek, M.; Malinowska, A.; Diduszko, R.; Wierzbicka, E.; Gogotsi, Y. Oxycarbide MXenes and MAX Phases Identification Using Monoatomic Layer-by-Layer Analysis with Ultralow-Energy Secondary-Ion Mass Spectrometry. *Nat. Nanotechnol.* **2022**, *17* (11), 1192−1197.

(52) Nowotny, H.; Rogl, P.; Schuster, J. C. Structural Chemistry of Complex Carbides and Related Compounds. *J. Solid State Chem.* **1982**, *44* (1), 126−133.

(53) Snyder, R. M.; Juelsholt, M.; Kalha, C.; Holm, J.; Mansfield, E.; Lee, T.-L.; Thakur, P. K.; Riaz, A. A.; Moss, B.; Regoutz, A.; Birkel, C. S. Detailed Analysis of the Synthesis and Structure of MAX Phase $(Mo_{0.75}V_{0.25})_5AlC_4$ and Its MXene Sibling $(Mo_{0.75}V_{0.25})_5C_4$. *ACS Nano* **2023**, *17* (13), 12693−12705.

(54) Shekhirev, M.; Busa, J.; Shuck, C. E.; Torres, A.; Bagheri, S.; Sinitskii, A.; Gogotsi, Y. Ultralarge Flakes of $Ti_3C_2T_x$ MXene via Soft Delamination. *ACS Nano* **2022**, *16* (9), 13695−13703.

(55) Raba, A. M.; Bautista-Ruíz, J.; Joya, M. R. Synthesis and Structural Properties of Niobium Pentoxide Powders: A Comparative Study of the Growth Process. *Mater. Res.* **2016**, *19*, 1381−1387.

(56) Mazza, T.; Barborini, E.; Piseri, P.; Milani, P.; Cattaneo, D.; Li Bassi, A.; Bottani, C. E.; Ducati, C. Raman Spectroscopy Characterization of TiO_2 Rutile Nanocrystals. *Phys. Rev. B* **2007**, *75* (4), No. 045416.

(57) Gouadec, G.; Colomban, P. Raman Spectroscopy of Nanomaterials: How Spectra Relate to Disorder, Particle Size and Mechanical Properties. *Prog. Cryst. Growth Charact. Mater.* **2007**, *53* (1), 1−56.

(58) Presser, V.; Naguib, M.; Chaput, L.; Togo, A.; Hug, G.; Barsoum, M. W. First-Order Raman Scattering of the MAX Phases: Ti_2AlN, $Ti_2AlC_{0.5}N_{0.5}$, Ti_2AlC, $(Ti_{0.5}V_{0.5})_2AlC$, V_2AlC, Ti_3AlC_2, and Ti_3GeC_2. *J. Raman Spectrosc.* **2012**, *43* (1), 168−172.

(59) Pelletier, M. J. *Analytical Applications of Raman Spectroscopy*; Blackwell Science: Oxford, 1999; Vol. 427.

(60) Sarycheva, A.; Gogotsi, Y. Raman Spectroscopy Analysis of the Structure and Surface Chemistry of $Ti_3C_2T_x$ MXene. *Chem. Mater.* **2020**, *32* (8), 3480−3488.

(61) Mathis, T. S.; Maleski, K.; Goad, A.; Sarycheva, A.; Anayee, M.; Foucher, A. C.; Hantanasirisakul, K.; Shuck, C. E.; Stach, E. A.; Gogotsi, Y. Modified MAX Phase Synthesis for Environmentally Stable and Highly Conductive Ti_3C_2 MXene. *ACS Nano* **2021**, *15* (4), 6420−6429.

(62) Blöchl, P. E. Projector Augmented-Wave Method. *Phys. Rev. B* **1994**, *50* (24), 17953−17979.

(63) Kresse, G.; Joubert, D. From Ultrasoft Pseudopotentials to the Projector Augmented-Wave Method. *Phys. Rev. B* **1999**, *59* (3), 1758−1775.

(64) Kresse, G.; Hafner, J. Ab Initio Molecular Dynamics for Liquid Metals. *Phys. Rev. B* **1993**, *47* (1), 558−561.

(65) Kresse, G.; Furthmüller, J. Efficiency of Ab-Initio Total Energy Calculations for Metals and Semiconductors Using a Plane-Wave Basis Set. *Comput. Mater. Sci.* **1996**, *6* (1), 15−50.

(66) Kresse, G.; Furthmüller, J. Efficient Iterative Schemes for Ab Initio Total-Energy Calculations Using a Plane-Wave Basis Set. *Phys. Rev. B* **1996**, *54* (16), 11169−11186.

(67) Perdew, J. P.; Burke, K.; Ernzerhof, M. Generalized Gradient Approximation Made Simple. *Phys. Rev. Lett.* **1996**, *77* (18), 3865−3868.

(68) Zunger, A.; Wei, S.-H.; Ferreira, L. G.; Bernard, J. E. Special Quasirandom Structures. *Phys. Rev. Lett.* **1990**, *65* (3), 353−356.

(69) Dahlqvist, M.; Rosen, J. Predictive Theoretical Screening of Phase Stability for Chemical Order and Disorder in Quaternary 312 and 413 MAX Phases. *Nanoscale* **2020**, *12* (2), 785−794.

(70) Dahlqvist, M.; Rosen, J. The Rise of MAX Phase Alloys − Large-Scale Theoretical Screening for the Prediction of Chemical Order and Disorder. *Nanoscale* **2022**, *14* (30), 10958−10971.

(71) Dahlqvist, M.; Alling, B.; Abrikosov, I. A.; Rosén, J. Phase Stability of Ti_2AlC upon Oxygen Incorporation: A First-Principles Investigation. *Phys. Rev. B* **2010**, *81* (2), No. 024111.

(72) Dahlqvist, M.; Alling, B.; Rosén, J. Stability Trends of MAX Phases from First Principles. *Phys. Rev. B* **2010**, *81* (22), 220102.

(73) Dai, Y.; Gao, J.; Huang, L.; Ding, R.; Wang, P.; Yang, F. First-Principles Study of Resistive Random Access Memory Based on Single-Layer Black Phosphorous Resistive Layer. *J. Appl. Phys.* **2020**, *128* (21), 215702.

(74) Thore, A.; Dahlqvist, M.; Alling, B.; Rosén, J. First-Principles Calculations of the Electronic, Vibrational, and Elastic Properties of the Magnetic Laminate Mn_2GaC. *J. Appl. Phys.* **2014**, *116* (10), 103511.

(75) Ingason, A. S.; Petruhins, A.; Dahlqvist, M.; Magnus, F.; Mockute, A.; Alling, B.; Hultman, L.; Abrikosov, I. A.; Persson, P. O. Å.; Rosen, J. A Nanolaminated Magnetic Phase: Mn_2GaC. *Mater. Res. Lett.* **2014**, *2* (2), 89−93.

(76) Dahlqvist, M.; Rosen, J. Order and Disorder in Quaternary Atomic Laminates from First-Principles Calculations. *Phys. Chem. Chem. Phys.* **2015**, *17* (47), 31810−31821.

https://doi.org/10.1021/acsnano.3c04967
ACS Nano 2023, 17, 17158−17168